3D Reconstruction of Tubular Structure Using Radially Deployed Projections

Unan, Mahmut
University of Alabama at Birmingham
unan@uab.edu

An, Junmo
University of Houston
jan2@uh.edu

Seimenis, Ionnis
Democritus University of Thrace
iseimen@med.duth.gr

Shah, Dipan J
Houston Methodist Hospital
djshah@houstonmethodist.org

Tsekos, Nikolaos V.
University of Houston
nvtsekos@central.uh.edu

Abstract

Acquiring volumetric data plays a crucial role in the field of medical imaging. 3D reconstruction is mostly performed using multislice image datasets. The objective of this research is to introduce a magnetic resonance technique for imaging tubular structures and their 3D reconstructions using multiple radially deployed projections. The oblique projection sequence was evaluated on a phantom, and multislice dataset is collected using the same phantom for the reference. To compute the correctness of the 3D reconstruction process, the resulting meshes were compared using the Hausdorff Distance Calculation and Point Cloud Comparison methods.

Keywords: Magnetic Resonance Imaging, 3D Reconstruction, Oblique Projections

1. Introduction

Volumetric imaging plays a vital role in the medical diagnosis and treatment. It is widely used for 3D visualization of tubular structures such as blood vessels [1], catheters [2], and bones [3]. 3D reconstruction is created by using different medical imaging modality outputs such as dual plane fluoroscopy [4, 5], biplane x-ray [1, 3, 6], CT [7] and MRI [2, 8].

The traditional 3D reconstruction techniques in the field of medical imaging generate 3D volume from a set of 2D stacked images. These techniques use different rendering algorithms on data volume such as Multiplanar Rendering (MPR), Surface Rendering (SR), and Volume Rendering (VR). Due to requiring a significant amount of time, creating 3D volume from the multislice dataset is not a time-efficient technique. 3D reconstruction from two or more projection images is a common technic especially in dual plane fluoroscopy [5] and biplane x-ray angiography [6]. However, due to having ionizing radiation and the existing co-registration problems, these imaging modalities are not impeccable. Magnetic Resonance Imaging (MRI) is a substantial and many-sided medical imaging modality. MRI uses the rules of Nuclear Magnetic Resonance combined with gradient coil elements to offer spatial encoding; as a result, it has the ability to perform three-dimensional imaging of the organism [9,10]. Even though MRI enables one to obtain more details in the soft tissues and has the capability of multiplanar imaging, it takes more time to perform it.

3D reconstruction from two projections is a common method in biplane fluoroscopy [11]. Dual plane fluoroscopy projections are not orthogonal to each other and the centers of the corresponding field of views are not identical. Thus, a series of transformations is computed to co-register these projections to the same coordinate system of reference. On the contrary while using MRI, multiple projections are already inherently co-registered, and the center and size of the field of views are the same [12].

3D Reconstruction of the tubular structures using three orthogonal MRI projection images were studied and the weakness of the triplanar method is analyzed [13]. For the complex structures, three orthogonal images are not sufficient and the overlapped structures are resulting in the ghost shapes.

The Radon Transform of an image is a set of projections of the image taken at different angles. This method has been used in widespread applications in medical imaging. Inverse Radon Transform (I-Radon) is to reconstruct the original image from its projections along various directions [14].

In this particular work, we collected MRI projection data from different angles and applied I-Radon transform method to acquire 3D Reconstruction of the tubular structure. In order to analyze the correctness of the reconstructed object, we collected multislice dataset from the same object and applied rendering algorithm to extract a reference object out of this dataset. The correctness is tested via two different methods; Hausdorff Distance Calculation and Point Cloud Comparison methods.

2. Data Acquisition

The oblique projection sequence was evaluated on a phantom made of a Gd-filled (3% Gd-doped water) tube (3.0 mm inner diameter and 4.0 mm outer diameter) embedded into a watery yogurt-based matrix. Studies were performed on a 1.5T PHILIPS MRI scanner using the body coil for both transmission and reception. After positioning and securing the phantom, scout images were collected to identify the volume of interest. Then 32 projection images were collected along the Y axis with a T1-weighted steady-state precession (FFE) pulse sequence (pixel spacing=0.958333 mm, flip angle = 50°, bandwidth/pixel = 190 Hz, matrix size = 230X230, FOV = 200X200 mm2, slice thickness = 200 mm, repetition time = 5.3650 ms, echo time= 1.601 ms, number of phase encoding steps = 230, echo training length = 92, percent sampling = 98.9247, percent phase field of view = 80, acquisition duration = 32.99 ms, bits allocated = 16, and bits stored = 12). For reference (i.e. the ground truth), we then collected a multislice set composed of 142 coronal slices with a standard inversion recovery gradient recalled echo (IR-GRE) sequence (flip angle = 30°, bandwidth/pixel = 172 Hz, matrix size = 256X256, fov = 200X200 mm2, slice thickness = 1.8 mm, pixel spacing = 0.71875 mm, repetition time = 25, echo time= 4.047, number of phase encoding steps= 257, echo training length = 1, percent sampling = 78.53981, percent phase field of view = 78.75, acquisition duration = 176.375, and acquisition time TM= 164141.55). The data were then stored and processed off-line with the reconstruction software, Osirix.

Projection images were placed on the 3D coordinate system regarding their position and orientation information in the DICOM header file. Figure 1 shows the 32 projection images placed on the 3D coordinate system.

Figure 2 shows the multislice dataset placed in the 3D coordinate system. There are 142 images scanned through the Z axis. Figure 3 presents the Maximum Intensity Projection (MIP) of the multislice dataset. MIP is a visualization method used in CT to detect nodules in lung cancer, and it consists of projecting the voxel with the maximum attenuation value on every view throughout the volume onto a 2D image.

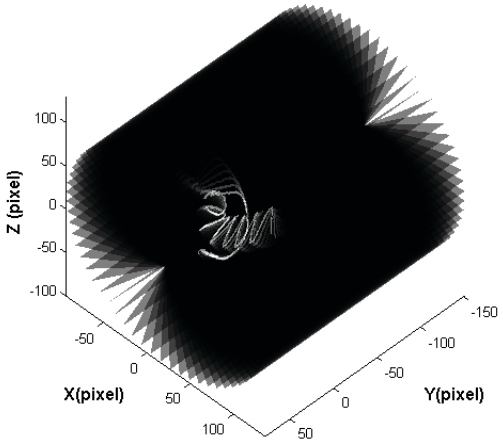

Figure 1:The projection images placed in 3D coordinate system

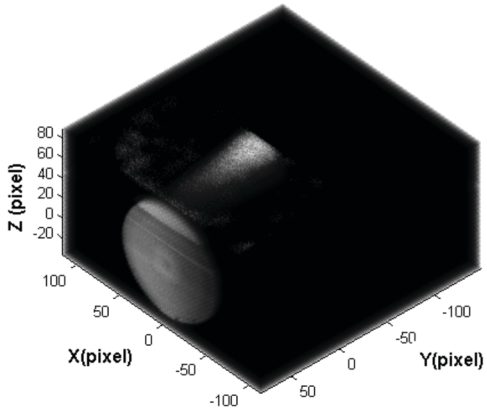

Figure 2:The multislice dataset placed in 3D coordinate system

Figure 3:Maximum Intensity Projection of the multislice dataset

3. Data Processing

In order to increase the contrast of the projection images, we applied an unsharp filter to each image. It is a sharpening technique used to enhance the edges of an image. The unsharp filter subtracts the smoothed version of an image from the original image. After applying the unsharp filter, we created a binary mask for each projection image. These binary masks had some noise after the conversion, thus we removed small objects using a MATLAB built-in function; bwareopen().
DICOM header information of the original projection images were copied to create new DICOM files from the binary images. Figure 4 displays some of the original projection images and their binary mask. The rotation of the image orientation can be observed from these figures.

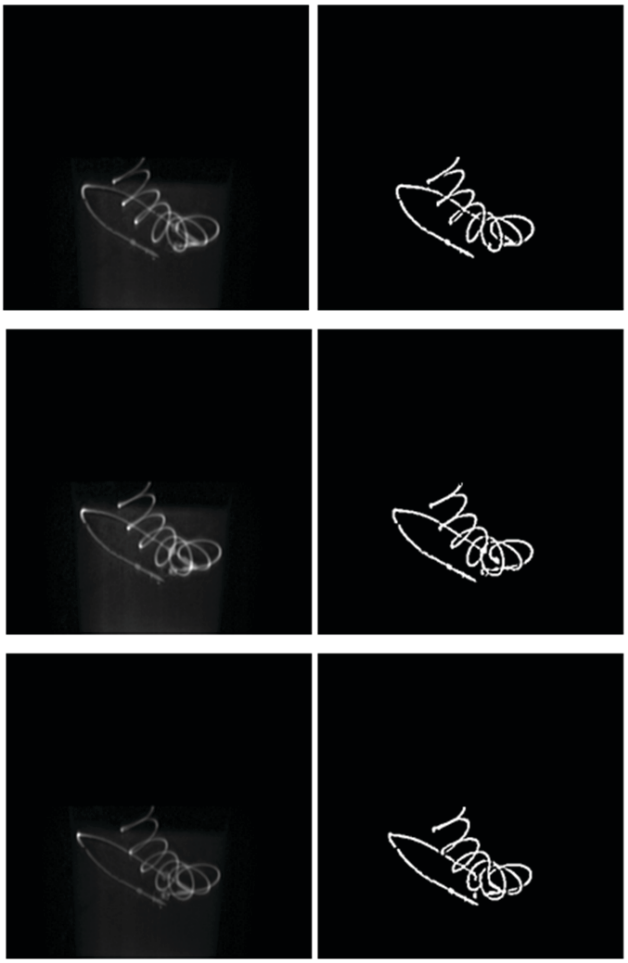

Figure 4:Original projection images and their binary masks, from image 6 to 8

4. Data Reordering

Projection images were collected for every 5.625 degrees around the Y axis of the same region of interest as illustrated in Figure5A. I-Radon transform method works for the 2 dimensions; thus, we reordered the data and applied the I-Radon algorithm for each slice in the new order (Figure 5B). The angle between each slice is calculated using the following formula;

$$Angle\ between\ projection\ images = \left(\frac{180}{Number of\ projections}\right)$$

The angle value of each image was stored in a vector variable and was used in the I-Radon Transform. The way we programmed the MRI scanner to collect the data was equivalent to applying the Radon Transform to the imaged object. Therefore, to generate the original object we implemented I-Radon Transform. A CT scanner does exactly this thing.

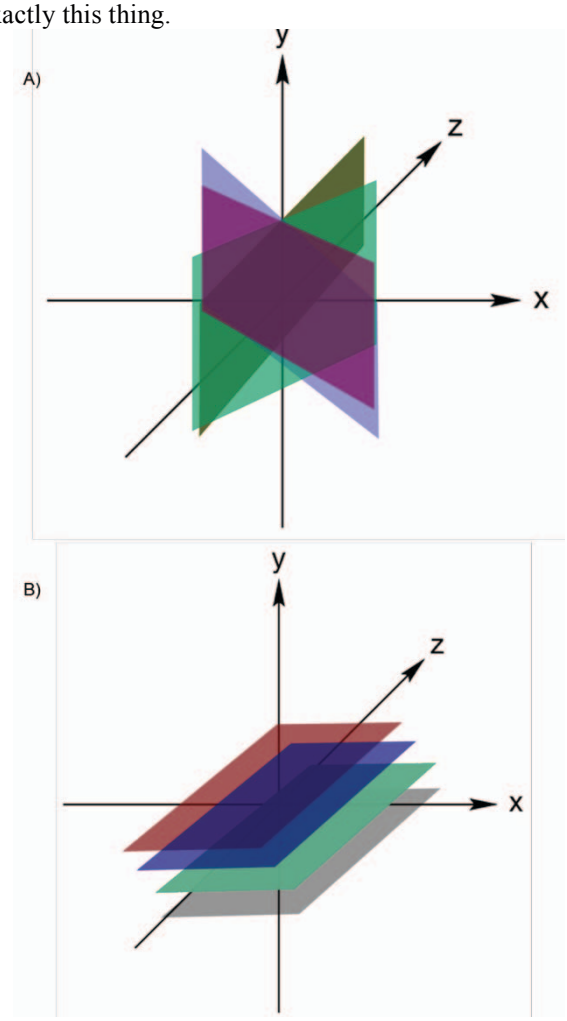

Figure 5:Illustration of the data reordering; A) Projection images in the 3D coordinate system B) Reordered projection images

Projection images were stored in a 3d matrix in accordance with the angle of rotations. The size of the projection matrix was 360x360x32. The projection matrix was reordered to create a new matrix for the I-Radon Transform.

The reordering algorithm is shown in the Table 1 (NRotationAxis (Number of Rotation Axis) =360, NOrthogonalAxis (Number of Orthogonal Axis) =360, and NProjections (Number of Projection Images) =32).

Table 1: Algorithm for Matrix Reordering

input: *imageMatrix (*NRotationAxis*,* NOrthogonalAxis*,* NProjections*)* **output:** *iRadonMatrix (*NOrthogonalAxis*,* NProjections*,* NRotationAxis*)*
1. for i= 1 to NRotationAxis
2. for k = 1 to NProjections
3. for j = 1 to NOrthogonalAxis
4. iRadonMatrix (j, k, i) = imageMatrix (i, j, k)
5. end for: j
6. end for: k
7. end for: i

The resulting 3D matrix was the size of 360x32x360. We selected slices along the (j, k) axis and applied the I-Radon Transform for each slice (360 slices).

5. Inverse Radon Transform

We selected images from the iRadonMatrix through the i axis and applied Inverse Radon Transform for these images. We used MATLAB iradon function with the following parameters; interpolation = spline, filter= Hamming. The output of the iradon function is a 2D image of the 2D reconstruction. These output images had some noise depending on the number of projections used in the I-Radon Transform. While the number of the projection images were increased, the level of the noise reduced. The output images were converted into binary images with an appropriate threshold level to eliminate the noise. The binary results were stored in another 3D matrix and the resulting 3D object mesh was reconstructed out of this matrix (Figure 6). To test the correctness of the reconstruction, we used the object reconstructed from the multislice dataset. Osirix software was used to process the multislice data set and the resulting object was saved as a mesh file. Figure 29 shows the resulting object mesh of the multislice data set after the surface rendering algorithm was applied (Figure 7). Figure 8 shows the superimposed 3D rendering of both structures.

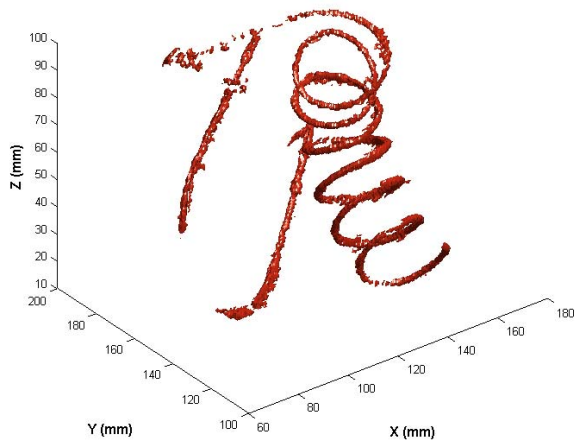

Figure 6: The output mesh of the I-Radon transformation of the 32 projection images

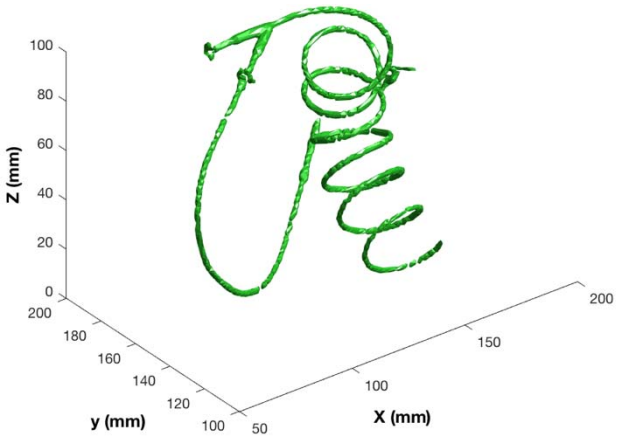

Figure 7: The mesh of the multislice dataset

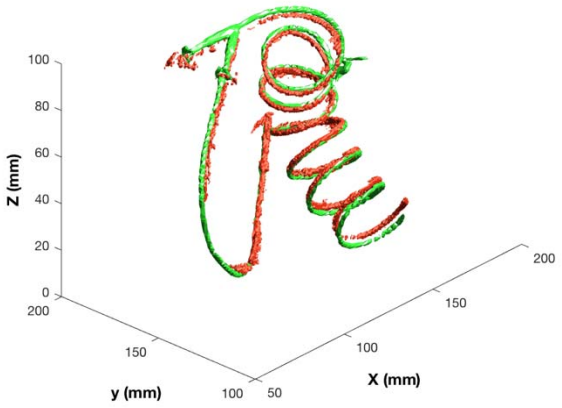

Figure 8: Superimposed 3D rendering of I-Radon Transformation and Multislice Surface Rendering

6. Results

Point Cloud Comparison method and Hausdorff Distance Calculation method was used to compare the resulting two meshes. Two meshes converted into point clouds using 1,000,000 points for each mesh. The Euclidian distance was calculated for each point. The distance values are grouped in the 8 classes to display the error rate. Table 2 shows the result of the Point Cloud Comparison method.

Table 2: The result of the Point Cloud Comparison method

Class	Class starts (mm)	Class ends (mm)	Number of points	Number of points (%)
1	0.002145543	0.924665254	408592	*40.85*
2	0.924665254	1.847184966	254145	*25.41*
3	1.847184966	2.769704678	166667	*16.66*
4	2.769704678	3.69222439	98852	*9.88*
5	3.69222439	4.614744102	56148	*5.61*
6	4.614744102	5.537263814	13170	*1.31*
7	5.537263814	6.459783526	1701	*0.17*
8	6.459783526	7.382303238	520	*0.05*

To convert mesh to point cloud, we used 1,000,000 points. The percentage of the points in a specific class is calculated by dividing the number of points in that class into 1,000,000. As shown on the table, more than 40% of the points have less than 1 mm and more than 82% of the points have less than 2.77 mm error rate. Although the maximum error is 7.38 mm, the ratio of these points is only 0.05%. We might say that the unfiltered noise caused of these results.

In addition, Figure 9 displays these results on the bar graph. As displayed on the graph that the majority of the points (~70%) have less than 2 mm distance.

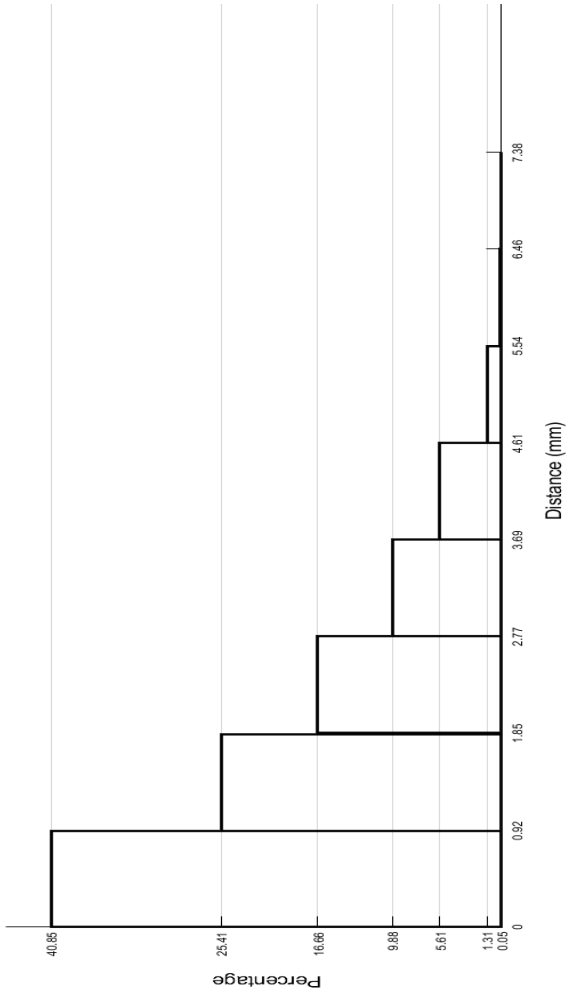

Figure 9: The result of the Point Cloud Comparison method

Furthermore, Hausdorff Distance Calculation method was computed, and the result is shown in the Table 3. As shown on the table, the Point Cloud Comparison method produced similar results to Hausdorff Distance Calculation method. The average error was 1.52 mm according to these two methods.

Table 3: The results of the Hausdorff Distance Calculation and Point Cloud Comparison methods

	Minimum (mm)	Maximum (mm)	Mean (mm)	Std
Point Cloud	0.00000	7.382300	1.525150	1.230497
Hausdorff	0.000031	7.281123	1.525351	1.247692

7. Discussions

Oblique orientation images were acquired around the Y axis for each 5.625 degree (32 images). The projection images were converted into binary masks and stored in a 3D matrix. The output of the 3D I-Radon was converted into a mesh file, and a 3D object was reconstructed. The correctness of this method was also tested with the result of the multislice dataset. Hausdorff and Point Cloud methods generated similar results for the average error rate (1.52 ± 1.27 mm vs 1052 ± 1.23 mm, respectively). Oblique projection images had enough contrast to automate the binary mask creation. I-Radon method was modified and implemented for 3D reconstruction of the structure using oblique projection images. The results of this experiment show that the number of projection was a vital parameter of this method. Fewer projection images created more noise; thus, it was not possible to 3D reconstruct the structure.

As one can appreciate from Figure 8, at the lower portion of the two reconstructions, two structures deferred. We suspected that the pulse sequence we implemented did not generate accurately balanced gradients and Y and Z axis gradients were calculated with different weighting parameters. As a result, we had differential scaling factors along the two axes on the reconstructed structure. The solution to this problem is rather trivial but time consuming. Specifically, we plan extensive studies with a phantom to calibrate MR scanner. Also, it can be noticeable from Figure 8 that there is a significant portion of the reconstructed object is missing. We figured out that this error occurs because of the plastic connector of the catheter that we used in the phantom study. Plastic connector is invisible in the projection images; thus it is impossible to reconstruct that part.

8. Acknowledgements

This work was supported in part by the National Science Foundation grant CNS-1646566, a Greek Diaspora Fellowship granted by the Stavros Niarchos Foundation and administered by the Institute of International Education. All opinions, findings, conclusions or recommendations expressed in this work are those of the authors and do not necessarily reflect the views of our sponsors.

9. References

[1] Pellot, C., Herment, A., Sigelle, M., Horain, P., Maitre, H., and Peronneau, P., 'A 3d Reconstruction of Vascular Structures from 2 X-Ray Angiograms Using an Adapted Simulated Annealing Algorithm', *IEEE Transactions on Medical Imaging*, 1994, 13, (1), pp. 48-60.

[2] Schirra, C.O., Weiss, S., Krueger, S., Caulfield, D., Pedersen, S.F., Razavi, R., Kozerke, S., and Schaeffter, T., 'Accelerated 3D catheter visualization from triplanar MR projection images', *Magnetic Resonance in Medicine*, 2010, 64, (1), pp. 167-176.

[3] Gunay, M., Shim, M.B., and Shimada, K., 'Cost- and time-effective three-dimensional bone-shape reconstruction from X-ray images', *The International Journal of Medical Robotics Computer Assisted Surgery*, MRCAS, 2007, 3, (4), pp. 323-335.

[4] Zheng, G.Y., Nolte, L.P., and Ferguson, S.J., '2D/3D Reconstruction of A Scaled Lumbar Vertebral Model from A Single Fluoroscopic Image', *2010 Annual International Conference of the IEEE Engineering in Medicine and Biology Society (EMBC)*, 2010, pp. 4395-4398.

[5] Bingham, J., and Li, G. 'An optimized image matching method for determining in-vivo TKA kinematics with a dual-orthogonal fluoroscopic imaging system', *Journal of Biomechanical Engineering*, 2006, 128, (4), pp. 588-595.

[6] Klein, J.L., Hoff, J.G., Peifer, J.W., Folks, R., Cooke, C.D., King, S.B., and Garcia, E.V. 'A quantitative evaluation of the three dimensional reconstruction of patients' coronary arteries', *International Journal of Cardiac Imaging*, 1998, 14, (2), pp. 75-87.

[7] Al Moussawi, A., Galusinski, C., and Nguyen, C. '3D Reconstruction of blood vessels', *Engineering with Computers*, 2015, 31, (4), pp. 775-790.

[8] Atalar, E., Kraitchman, D.L., Carkhuff, B., Lesho, J., Ocali, O., Solaiyappan, M., Guttman, M.A., and Charles, H.K. 'Catheter-tracking FOV MR fluoroscopy', *Magnetic Resonance in Medicine*, 1998, 40, (6), pp. 865-872.

[9] Kramer, D.M., Schneider, J.S., Rudin, A.M., and Lauterbur, P.C., 'True three-dimensional nuclear magnetic resonance zeugmatographic images of a human brain', *Neuroradiology*, 1981, 21, (5), pp. 239-244.

[10] Lauterbur, P., 'NMR imaging in biomedicine', *Cell Biophysics,* 1986, 9, (1-2), pp. 211-214.

[11] Baert, S.A., Van de Kraats, E.B., Van Walsum, T., Viergever, M.A., and Niessen, W.J., 'Three-dimensional guide-wire reconstruction from biplane image sequences for integrated display in 3-D vasculature', *IEEE Transactions on Medical Imaging*, 2003, 22, (10), pp. 1252-1258.

[12] Bender, H.J., Manner, R., Poliwoda, C., Roth, S., and Walz, M. 'Reconstruction of 3D catheter paths from 2D X-ray projections', *Medical Image Computing and Computer-Assisted Intervention*, Miccai'99, Proceedings, 1999, 1679, pp. 981-989.

[13] An, J., Unan, M., Chin, K., Shah, D.J., Webb, A.G., Seimenis, I., and Tsekos, N.V., '3D Reconstruction of Tubular Structures from Three Orthogonal MRI Projections', *XIV Mediterranean Conference on Medical and Biological Engineering and Computing 2016*, 2016, 57, pp. 326-331.

[14] Mitra, A., and Banerjee, S., 'A regular algorithm for real time radon & inverse radon transform', *2004 IEEE International Conference on Acoustics, Speech, and Signal Processing*, Vol V, Proceedings, 2004, pp. 105-108.